

# Contents

Abstract (in Chinese)	i
Abstract (in English)	iv
Acknowledgments (in Chinese)	viii
Contents	ix
Table Lists	xv
Figure Captions	xvii

## ***Chapter 1 Introduction.....1***

1.1	Brief of Power Device Design.....	1
1.2	Current Status of Power Semiconductor Devices.....	3
1.2.1	Power MOSFETs.....	3
1.2.2	Insulated Gate Bipolar Transistors (IGBTs).....	4
1.2.3	Examples of Power Devices Applications.....	6
1.2.4	Power Device Reliability.....	8
1.3	Evolution of Power Semiconductor Technology.....	9
1.3.1	High Voltage Integrated Circuit (HVIC).....	9
1.3.2	System-on-a-Chip (SOC) and Three-Dimensional Integration.....	10
1.3.3	Technology Options.....	11
1.4	Motivation.....	13

## ***Chapter 2 Investigation of Conventional Single-Crystalline Silicon-On-Insulator Lateral -Double-Diffused-Metal-Oxide-Semiconductor (SOI Lateral- DMOS) Fabrication by Bipolar-Complementary***

## ***MOS-DMOS Process on Bulk Silicon***

<b><i>Substrate</i></b> .....	<b>18</b>
2.1 Introduction for BCD and SOI BCD.....	19
2.2 Device Fabrication.....	21
2.3 Results and Discussion.....	24
2.3.1 Thickness Consideration of SOI Active Layer.....	24
2.3.2 Dependence of Breakdown Voltage on Drift Length and Drain Metal Extension.....	26
2.3.3 Safe Operating Area for Compatible BCD SOI-LDMOS.....	28
2.3.4 Transient Characteristics of Compatible BCD SOI-LDMOS.....	30
2.3.5 RF Characteristics of Compatible BCD SOI-LDMOS.....	34
2.3.6 Compatible High-Voltage BCD SOI-LDMOS for High-Frequency Applications.....	38
2.4 Summary.....	41

## ***Chapter 3 Modeling and Design of the High Performance Step-Doping Silicon On Insulator Lateral Insulated Gate Bipolar Transistor (SOI-LIGBT) Power Devices by Partition Mid-Point Method....43***

3.1 Merits of Silicon-On-Insulator (SOI) devices.....	44
3.1.1 Linearly Graded Doping Profile for Superior Breakdown Voltage.....	44
3.1.2 Linearly Graded Doping SOI-LDMOS and SOI-LIGBT.....	48
3.1.2.1 Local Heating in Linearly Graded Doping SOI-LDMOS.....	48
3.1.2.2 Temperature Relaxation by Linearly Graded Doping SOI-LIGBT .....	50

3.1.3	Challenges for Linearly Graded Doping Design.....	51
3.2	Modeling Descriptions and Verifications.....	53
3.2.1	Comparison of Step Doping Profile and Linearly Graded Doping.....	53
3.2.2	General Equation of Step-Doping SOI-LIGBT.....	57
3.2.3	Specific Equation of Step-Doping SOI-LIGBT for Three Frames.....	62
3.2.3.1	Surface Potential at Top Si/SiO <sub>2</sub> Interface for Three Frames.....	64
3.2.3.2	Surface Electric Field at Top Si/SiO <sub>2</sub> Interface.....	69
3.3	Results and Discussion.....	73
3.3.1	Derivation of Breakdown Voltage and Issue Location.....	73
3.3.2	Analytical Results Compared with MEDICI Simulation.....	74
3.3.3	Deviation between Analytical Model and MEDICI Simulation.....	79
3.4	Summary.....	82

**Chapter 4 A LDMOS with Low-Temperature Poly-Si Power Device via  
Excimer Laser Crystallization at Room Temperature.....84**

4.1	Poly-Si Grain Growth Technology.....	84
4.1.1	Solid Phase Crystallization (SPC).....	84
4.1.2	Excimer Laser Crystallization (ELC).....	85
4.2	Conventional SPC HVTFTs and Novel ELC HVLD MOS.....	86
4.3	Device Fabrication.....	91
4.4	Results and Discussion.....	94
4.4.1	X-Ray Diffraction and SEM Photography.....	94
4.4.2	Transfer Characteristics before/after Excimer Laser Treatments for LTPS HVLD MOS.....	96
4.4.3	Relationship between ON/OFF Current Ratio and Drift Length before/after	

Excimer Laser Treatments for LTPS HVLD MOS.....	98
4.4.4 Output Characteristics before/after Excimer Laser Treatments for LTPS HVLD MOS.....	103
4.4.5 Comparison of LTPS HVLD MOS before/after Laser Treatments together with Conventional OD, MFP, and SI HVTFTs.....	105
4.5 Summary.....	107

**Chapter 5 LDMOS Devices of Low-Temperature Polycrystalline-Silicon**

***Crystallized at 400 °C Substrate Heating.....109***

5.1 Advanced LTPS LDMOS for 400 °C Irradiation.....	109
5.2 Experiments.....	111
5.3 Results and Discussion.....	114
5.3.1 Transfer Characteristics of Conventional OD TFT and Novel LTPS LDMOS with Room Temperature Irradiation.....	114
5.3.2 Transfer Characteristics of LTPS LDMOS at RT and 400 °C Irradiations.....	115
5.3.3 Relationship between ON/OFF Current Ratio and Drift Length of LTPS LDMOS at RT and 400 °C Irradiations.....	118
5.3.4 Output Characteristics of LTPS LDMOS at RT and 400 °C Irradiations.....	121
5.3.5 Comparison of LTPS LDMOS at RT and 400 °C Irradiations together with OD and VDS TFTs.....	124
5.3.5.1 Specific On-Resistance.....	124
5.3.5.2 Breakdown Voltage.....	125
5.4 Summary.....	127

**Chapter 6 Thermal Analyses on Single-Crystalline and Low- Temperature Polycrystalline Silicon Power Devices.....129**

6.1 Self-Heating Effects in SOI Devices.....130

6.2 Comparison of Leakage Currents in Bulk and Different-Thickness SOI Devices at High Temperature Operation.....133

6.3 Experiments.....134

6.4 Results and Discussion.....137

6.4.1 Transfer Characteristics of LTPS LDMOS at RT and 400 °C Irradiations over Ambient Temperature Range of 300–400 K.....137

6.4.1.1 Relationship between ON/OFF Currents and Ambient Temperatures for LTPS LDMOS.....137

6.4.1.1.1 ON and OFF Currents at Drain Bias of 0.1 V.....137

6.4.1.1.2 ON/OFF Current Ratios at Drain Bias of 0.1 V.....139

6.4.1.1.3 ON and OFF Currents at Drain Bias of 10 V.....141

6.4.1.1.4 ON/OFF Current Ratios at Drain Bias of 10 V.....143

6.4.1.2 Relationship between Threshold Voltages and Ambient Temperatures for c-Si LDMOS and LTPS LDMOS.....145

6.4.1.3 Relationship between Subthreshold Swings and Ambient Temperatures for c-Si LDMOS and LTPS LDMOS.....148

6.4.2 Output Characteristics of LTPS LDMOS at RT and 400 °C Irradiations over Ambient Temperature Range of 300–400 K.....152

6.4.2.1 Relationship between Specific On-Resistances and Ambient Temperatures for c-Si LDMOS and LTPS LDMOS.....152

6.4.2.2 Relationship between Breakdown Voltages and Ambient Temperatures for c-Si LDMOS and LTPS LDMOS.....156

6.5 Summary.....158

*Chapter 7 Summary and Conclusions.....160*

*Chapter 8 Future Prospects.....167*

*References.....172*

**Vita**

**Publication Lists**



# Table Lists

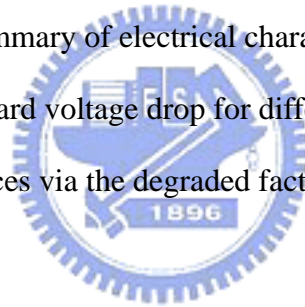
## *Chapter 2*

Table 2-1. Comparison of 12/25/5/40V Bulk-BCD and 450V SOI-LDMOS process flows.

Table 2-2. Summary of small-signal characteristics with the parameters of operation current, maximum frequency, and cutoff frequency from gate bias of 1-V to 12-V.

## *Chapter 3*

Table 3-1. Summary of electrical characteristics of breakdown voltage and forward voltage drop for different frames and grading doping devices via the degraded factors.



## *Chapter 4*

Table 4-1. Summary of the transfer characteristics before and after excimer laser treatments for LTPS HVLD MOS with optimal room temperature irradiation.

## *Chapter 5*

Table 5-1. Summary of the transfer characteristics for the conventional OD TFT and the proposed LTPS LDMOS under optimal room temperature irradiation.

Table 5-2. Summary of the transfer characteristics of LTPS LDMOS at room temperature and 400 °C irradiations with optimal laser conditions.

## ***Chapter 6***

Table 6-1. Summary of on and off currents for LTPS LDMOS at RT and 400 °C Irradiations with  $V_{ds}=0.1$  V and over Ambient Temperature Range of 300–400 K.

Table 6-2. Summary of ON/OFF current ratios for LTPS LDMOS at RT and 400 °C Irradiations with  $V_{ds}=0.1$  V and over Ambient Temperature Range of 300–400 K.

Table 6-3. Summary of on and off currents for LTPS LDMOS at RT and 400 °C Irradiations with  $V_{ds}=10$  V and over Ambient Temperature Range of 300–400 K.

Table 6-4. Summary of ON/OFF current ratios for LTPS LDMOS at RT and 400 °C Irradiations with  $V_{ds}=10$  V and over Ambient Temperature Range of 300–400 K.

Table 6-5. Summary of subthreshold swings for LTPS LDMOS at RT and 400 °C Irradiations over Ambient Temperature Range of 300–400 K.



# Figure Captions

## Chapter 2

- Fig. 2-1. SEM cross-sectional view of the compatible SOI-LDMOS with 4- $\mu\text{m}$  buried oxide, 5- $\mu\text{m}$  silicon film layer, 40- $\mu\text{m}$  drift length, 2.88- $\mu\text{m}$  p-well depth and 3.37- $\mu\text{m}$  n-buffer depth.
- Fig. 2-2. Breakdown voltage as a function of SOI thickness with buried oxide thickness as a parameter from  $t_{\text{OX}}=2\text{-}\mu\text{m}$  to  $t_{\text{OX}}=4\text{-}\mu\text{m}$ .
- Fig. 2-3. Calculated on-resistance as a function of SOI and buried oxide (BOX) thickness from  $t_{\text{OX}}=2\text{-}\mu\text{m}$  to  $t_{\text{OX}}=4\text{-}\mu\text{m}$ .
- Fig. 2-4. Dependence of breakdown voltage and forward voltage drop ( $V_{\text{ce}}$ ) on drift length extension of additional 25- $\mu\text{m}$  length.
- Fig. 2-5. Relationship of breakdown voltage and forward voltage drop at 10- $\mu\text{m}$  length drain metal with the variation from  $-5\text{-}\mu\text{m}$  to  $5\text{-}\mu\text{m}$ .
- Fig. 2-6. (a) Investigation of the SOA with the measured (DC thermal dissipation limit) and simulated (snapback boundary) maximum rated power limitations at room temperature.
- (b) Current variation after thermal damage as a function of terminal biases of drain-to-source, drain-to-gate, and gate-to-source.
- Fig. 2-7. (a) Schematic measurement circuit with HP 53181A frequency counter for contributing 1 KHz gate pulse, GW power supply for supplying high static drain voltage of 175-V, and TEK TDS5054 oscilloscope for detecting the output waveforms.
- (b) Illustration of turn-on switching waveforms during the gate transience from

low to high state with the delay time, propagation time, falls/rise time, and switch time of 11.4-ns, 150-ns, 410-ns, and 420-ns, respectively.

(c) Relationship between gate-to-source capacitances and gate-to-source voltages under different frequency measurements from Taurus extraction.

(d) Illustration of turn-off switching waveforms during the gate transience from high to low state with the delay time, propagation time, falls/rise time, and switch time of 280-ns, 930-ns, 2700-ns, and 3000-ns, respectively.

Fig. 2-8. (a) Establishment of corresponding maximum output swing at a drain voltage of 20-V between the experiment and simulation. The maximum voltage was set at drain bias of 40-V according to the maximum power limit of safe-operating area.

(b) Simulation of small-signal characteristics with respect to the cut-off frequencies  $f_T$  and  $f_{max}$  at various gate biases from two-dimensional (2-D) ATHENA/ATLAS (process/device) simulators.

Fig. 2-9. Low dissipation video amplifier application for high-resolution display by high voltage and high frequency device operations.

Fig. 2-10. Power LDMOS voltage source inverter in high frequency ballast system of high intensity discharge (HID) lamp for use in automobile headlamps application.

Fig. 2-11. Power MOSFETs in power factor correction (PFC) controller IC for use in low power (less than 150 Watt) switch mode power supply (SMPS) application.

### Chapter 3

Fig. 3-1. Simulation of uniform doping device for (a) 2-D potential curves and (b) 3-D electric field distribution at breakdown voltage of 402-V by Taurus extraction. The electric field distribution shows the two sharp edge triangular peaks and a large

middle dip in the drift region.

Fig. 3-2. Simulation of linearly graded doping device for (a) 2-D potential curves and (b) 1-D doping concentration distribution by Taurus extraction.

Fig. 3-3. Simulation of local heating effect in linearly graded doping device near the source side with (a) 2-D and (b) 1-D temperature distribution by Taurus extraction.

Fig. 3-4. Schematic diagram of temperature distribution in linearly graded doping SOI-LDMOS and SOI-LIGBT structures. The minor carrier in the SOI-LIGBT can relax the local heating effect.

Fig. 3-5. Fabrication of linearly graded doping profile with a precise sequence of slit openings for making impurity implantation and a long drive-in time at 1200 °C.

Fig. 3-6. Simulation of linearly graded doping device for (a) 3-D and (b) 1-D electric field distribution breakdown voltage of 617-V by Taurus extraction. The electric field in the middle of drift region is raised against a large dip for uniform doping profile.

Fig. 3-7. Simulation of step-doping device for (a) 2-D potential curves and (b) 3-D electric field distribution at breakdown voltage of 607-V by Taurus extraction. The additional electric peak appear at the step in the middle of drift region.

Fig. 3-8. Corresponding structure and frame architecture of step-doping SOI-LIGBT device. The concentration of the first frame is equal to the background doping which is also replicated from p-well to gate edge.

Fig. 3-9. Illustration of the partition method with a testing flowchart and single frame diagram. The key point is to determine whether the applied voltage will attain reach-throughout for each frame.

Fig. 3-10. Dependence of the breakdown voltage and frame number with degraded factor. The improvement of breakdown voltage is enough to use three frames in the drift region.

Fig. 3-11. Investigation of the optimum device characteristics in respect of breakdown

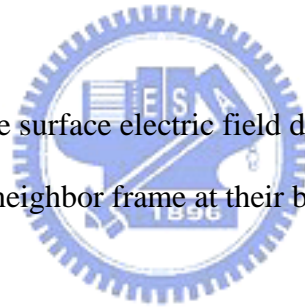
voltage and forward voltage drop with various numbers of frames. Its SOI layer thickness, buried oxide thickness, and the drift length are 1.5- $\mu\text{m}$ , 5- $\mu\text{m}$ , and 36- $\mu\text{m}$ , respectively.

Fig. 3-12. (a) Comparison of the surface potential distribution with analytical model and MEDICI simulation. The analytical result is most in agreement with the data generated by MEDICI simulation.

(b) The different kinds of surface electric field distribution are shown in each drift region before the breakdown voltage happens. The step doping type exhibits a significant electric improvement compared to the uniformly doping type.

Fig. 3-13. (a) Percentage of the surface potential deviation as a function of the distance in three frames. It is worth to mention that the maximum error value is occurred on the outset.

(b) Percentage of the surface electric field deviation as a function of the distance in three frames. Each neighbor frame at their boundary exist a higher error value.



## Chapter 4

Fig. 4-1. Schematic structure of offset-drain (OD) high-voltage thin film transistor (HVTFT) with a high resistance offset region from drain to source.

Fig. 4-2. Schematic structure of lightly doped drain (LDD) HVTFT with a lightly doping implantation in the offset region.

Fig. 4-3. Schematic structure of metal-field-plate (MFP) HVTFT with a metal field plate across the offset region.

Fig. 4-4. Schematic structure of multi-gate (MG) HVTFT with many gate elements between the drain and source region.

- Fig. 4-5. Schematic structure of semi-insulating (SI) HVTFT with connect of semi insulating field plate from drain to gate electrode over the offset region.
- Fig. 4-6. Key processes for fabricating the high performance LTPS HVLD MOS using excimer laser crystallization in the sequence of (a), (b), (c) and (d).
- Fig. 4-7. X-ray diffraction spectra of polycrystalline silicon film crystallized by excimer laser annealing with an energy density of  $470 \text{ mJ/cm}^2$  and a shot density of 100 per area at room temperature.
- Fig. 4-8. (a) Scanning electron microscopy (SEM) image of Secco-etched poly-Si film crystallized in the partial melting regime by a low energy density of  $435 \text{ mJ/cm}^2$  and a shot density of 100 per area at room temperature.
- (b) Scanning electron microscopy (SEM) image of Secco-etched poly-Si film crystallized in the super lateral growth (SLG) regime by a high energy density of  $458 \text{ mJ/cm}^2$  and a shot density of 100 per area at room temperature.
- Fig. 4-9. Transfer characteristics before and after excimer laser treatments for LTPS HVLD MOS with  $W/L_{\text{ch}}=600\text{-}\mu\text{m}/12\text{-}\mu\text{m}$  and  $L_{\text{drift}}=15\text{-}\mu\text{m}$ .
- Fig. 4-10. (a) Relationship between ON/OFF current ratio and drift length before and after excimer laser treatments for LTPS HVLD MOS at the drain bias of 5-V.
- (b) Relationship between ON/OFF current ratio and drift length before and after excimer laser treatments for LTPS HVLD MOS at the drain bias of 25-V.
- Fig. 4-11. Transfer characteristics before and after excimer laser treatments for LTPS HVLD MOS with  $W/L_{\text{ch}}=600\text{-}\mu\text{m}/12\text{-}\mu\text{m}$  and  $L_{\text{drift}}=20\text{-}\mu\text{m}$ .
- Fig. 4-12. Transfer characteristics before and after excimer laser treatments for LTPS HVLD MOS with  $W/L_{\text{ch}}=600\text{-}\mu\text{m}/12\text{-}\mu\text{m}$  and  $L_{\text{drift}}=25\text{-}\mu\text{m}$ .
- Fig. 4-13. Transfer characteristics before and after excimer laser treatments for LTPS HVLD MOS with  $W/L_{\text{ch}}=600\text{-}\mu\text{m}/12\text{-}\mu\text{m}$  and  $L_{\text{drift}}=35\text{-}\mu\text{m}$ .
- Fig. 4-14. Transfer characteristics before and after excimer laser treatments for LTPS

HVLDMOS with  $W/L_{ch}=600\text{-}\mu\text{m}/12\text{-}\mu\text{m}$  and  $L_{drift}=40\text{-}\mu\text{m}$ .

Fig. 4-15. (a) Output characteristics after excimer laser treatments with the linear scale drain current for LTPS HVLDMOS with  $W/L_{ch}=600\text{-}\mu\text{m}/12\text{-}\mu\text{m}$  and  $L_{drift}=15\text{-}\mu\text{m}$ . The breakdown voltage was measured by the protective current limit of 0.1 mA.

(b) Output characteristics before and after excimer laser treatments with the logarithm scale drain current for LTPS HVLDMOS with  $W/L_{ch}=600\text{-}\mu\text{m}/12\text{-}\mu\text{m}$  and  $L_{drift}=15\text{-}\mu\text{m}$ .

Fig. 4-16. Relationships of the specific on-resistance and breakdown voltage in the LTPS HVLDMOS before/after laser treatments against the previous OD, MFP, and SI HVTFTs. The numbers in brackets (x, y) represented the coordinates in X-axis and Y-axis, which meant the values of breakdown voltage and specific on-resistance, respectively.



## Chapter 5

Fig. 5-1. Schematic structure of various doping slit (VDS) thin film transistor (TFT) with a continuous shallow doping profile in the offset region.

Fig. 5-2. LTPS LDMOS structure fabricated by excimer laser crystallization under room temperature or 400°C irradiation. The broken circles represented the RESURF design and the solid circles indicated the drift with/without doping for reducing the resistance of drift region in LTPS LDMOS and OD TFT devices.

Fig. 5-3. Transfer characteristics of LTPS LDMOS for optimal room temperature and 400 °C irradiations with  $W/L_{ch}=600\text{-}\mu\text{m}/12\text{-}\mu\text{m}$  and  $L_{drift}=15\text{-}\mu\text{m}$ .

Fig. 5-4. (a) Dependence of on and off currents on the drift length variation from 15- $\mu\text{m}$  to 30- $\mu\text{m}$  at drains bias of 5 V for LTPS LDMOS at optimal room temperature and

400 °C irradiations.

(b) Relationship between of ON/OFF current ratios and the drift length variation from 15- $\mu\text{m}$  to 30- $\mu\text{m}$  at drains bias of 5 V for LTPS LDMOS at optimal room temperature and 400 °C irradiations.

Fig. 5-5. (a) Output characteristics of LTPS LDMOS for optimal room temperature and 400 °C irradiations. The circle was indicated the maximum power limit point of 1.11 Watts.

(b) Corresponding safe operating area (SOA) with the algorithmic scales of drain current and voltage.

(c) Output characteristics of LTPS LDMOS for optimal room temperature and 400 °C irradiations. The breakdown voltages were measured by the protective limits of 0.1 mA and 0.05 mA for room temperature and 400°C irradiations, respectively.

Fig. 5-6 (a) Relationships of the specific on-resistance and laser energy density for LTPS LDMOS at RT/400 °C irradiations together with OD TFT, VDS TFT and c-Si LDMOS. The optimal laser conditions were located at 470  $\text{mJ}/\text{cm}^2$  and 435  $\text{mJ}/\text{cm}^2$  for room temperature and 400 °C, respectively.

(b) Comparison of the breakdown voltages for the LTPS LDMOS at RT/400 °C irradiations together with OD TFT, VDS TFT, and c-Si LDMOS.

## Chapter 6

Fig. 6-1. (a) Contact through buried oxide layer (CTBOX) technique process flow.

(b) Power devices using a backside drain contact, heat sink, and even a forced air-cooling fan to help in dissipating the heat generation.

Fig. 6-2. (a) Key process for fabricating the novel LTPS LDMOS using excimer laser

crystallization with dimension of  $W/L_{ch} = 600\text{-}\mu\text{m}/12\text{-}\mu\text{m}$  plus a  $15\text{-}\mu\text{m}$  drift region.

(b) Instruments for measuring the novel LTPS LDMOS using excimer laser crystallization with  $w = 100\text{-V}/w = 100\text{-mA}$  HP4156C, 1100V KEITHLEY model 237, and  $-65\text{ }^{\circ}\text{C}\sim 400\text{ }^{\circ}\text{C}$  Micromanipulator H1000 high performance series thermal chuck systems.

Fig. 6-3. Relationship between on and off currents and ambient temperature variation from 300 K to 400 K at drains bias of 0.1 V for LTPS LDMOS at optimal room temperature and 400 °C irradiations.

Fig. 6-4. Relationship between ON/OFF current ratios and ambient temperature variation from 300 K to 400 K at drains bias of 0.1 V for LTPS LDMOS at optimal room temperature and 400 °C irradiations.

Fig. 6-5. Relationship between on and off currents and ambient temperature variation from 300 K to 400 K at drains bias of 10 V for LTPS LDMOS at optimal room temperature and 400 °C irradiations.

Fig. 6-6. Relationship between ON/OFF current ratios and ambient temperature variation from 300 K to 400 K at drains bias of 10 V for LTPS LDMOS at optimal room temperature and 400 °C irradiations.

Fig. 6-7. Dependence of the threshold voltages on ambient temperatures from 300 K-400K at 25 °C intervals for LTPS LDMOS at optimal room temperature and 400 °C irradiations.

Fig. 6-8. Dependence of the subthreshold swings on ambient temperatures from 300 K-400K at 25 °C intervals for LTPS LDMOS at optimal RT and 400 °C irradiations.

Fig. 6-9. (a) Transfer characteristics of LTPS LDMOS at drain bias of 0.1 V for optimal room temperature irradiation over ambient temperature from 300-K to 400-K.



(b) Transfer characteristics of LTPS LDMOS at drain bias of 0.1 V for optimal 400 °C irradiation over ambient temperature from 300-K to 400-K.

(c) Transfer characteristics of LTPS LDMOS at drain bias of 10 V for optimal room temperature irradiation over ambient temperature from 300-K to 400-K.

(d) Transfer characteristics of LTPS LDMOS at drain bias of 10 V for optimal 400 °C irradiation over ambient temperature from 300-K to 400-K.

Fig. 6-10. Specific on-resistances of LTPS LDMOS at room temperature and 400 °C irradiations over the ambient temperature from 300-K to 400-K.

Fig. 6-11. (a) Output characteristics of LTPS LDMOS for optimal RT irradiation at gate biases of 15-V and 25-V over ambient temperature from 300-K to 400-K.

(b) Output characteristics of LTPS LDMOS for optimal 400 °C irradiation at gate biases of 15-V and 25-V over ambient temperature from 300-K to 400-K.

Fig. 6-12. Breakdown voltages of LTPS LDMOS at room temperature and 400 °C irradiations over the ambient temperature from 300-K to 400-K.

